Solar Energy 291 (2025) 113344

Contents lists available at ScienceDirect

Solar Energy

journal homepage: www.elsevier.com/locate/solener

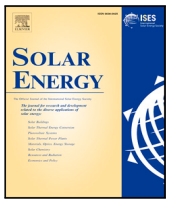

Deriving the orientation of existing solar energy systems from LiDAR data at scale

David Lingfors [a,*], Robert Johansson [b], Johan Lindahl [b]

[a] Department of Civil and Industrial Engineering, Uppsala University, SE-751 21 Uppsala, Sweden
[b] Becquerel Sweden AB, SE-741 42 Knivsta, Sweden

ARTICLE INFO

Keywords:
Photovoltaics
Solar thermal
Orientation
Remote sensing
LiDAR
Aerial images

ABSTRACT

Solar photovoltaics (PV) is currently the fastest growing type of electrical energy generation. A substantial share is distributed, and key information – such as their installed capacity, precise location, tilt, and azimuth – are often lacking or inaccurate. Therefore, obtaining accurate data on existing PV systems become increasingly critical to determine optimal locations for adding new PV capacity, in terms of ensuring grid stability. Recent advances in identifying and segmenting solar energy systems, using aerial imagery, point to a logical next step; enhancing the modelling of tilts and azimuths, as these influence the power output significantly. Therefore, a method is proposed that derives the tilt and azimuth of solar energy systems using Light Detection and Ranging (LiDAR) data. Polygons representing solar energy systems, identified in aerial images, are orthorectified to LiDAR data and then linear regression is applied to determine the orientation. The method is evaluated for 3'500 Swedish solar energy systems previously identified in aerial images, with a manually derived ground truth azimuth dataset. For 91%–95% of the systems, the model accurately estimated the azimuth within a margin of 3°. Furthermore, the distribution of azimuths was more narrow for solar thermal systems than for PV systems. A ground truth of the tilt for a subset of 39 systems gave a mean absolute error of 3.6°. The proposed method is believed to provide more accurate PV metadata to, e.g., aggregators and grid operators, enabling more precise PV power simulations and forecasts, in turn leading to better grid operation and planning.

1. Introduction

In 2023, solar PV power accounted for 457.6 GW or over 65% of all new electricity generation capacity additions worldwide, bringing the total cumulative capacity to approximately 1.6 TW [1]. The variability of the solar resource poses significant challenges to integrating large shares of PV power into the grid. These fluctuations impact the stability of the power system and must be managed effectively to maintain grid reliability [2]. As the penetration of distributed PV systems grows, the need to accurately forecast and understand both the total generated PV power and the self-consumed at aggregated local and regional levels becomes increasingly critical [3]. This will be essential for optimizing the operation of the electricity system and ensuring efficient energy management.

The orientation, i.e., tilt and azimuth, of a PV system highly influence the PV power output. Although installed capacity is often reported in PV databases, tilt and azimuth are most often not reported. For instance, in [4], PV metadata representing 14.8% of the world's installed capacity (by 2017), where analysed. Tilts and azimuths were only reported for 1.7% of the installed capacity, meaning that the orientation needs to be modelled or assumed in some way or another. Various strategies have been developed to address the unknown orientation of distributed PV systems in wide-area simulations. These include: (1) setting the tilt and azimuth angles to close the optimal orientation for maximum power generation at the location [5,6], (2) determining a single orientation for the entire fleet of PV systems by minimizing the discrepancies between simulated PV power and the actual regional power measured by a system operator [7], (3) using statistical methods to model the orientation distribution based on existing PV systems [8], or on the existing rooftops with the highest solar irradiation [9], (4) machine learning [10], or parametrization models based on reported PV power generation [11], or (5) novel remote sensing approaches, such as combining information extracted from aerial images with either 3D building data [12], or calibrating the tilt from the average of nearby systems found in a non-profit database [13].

If the aggregated PV power output across a region is of main interest, statistical methods to derive representative tilts, azimuths and/or capacity factors are sufficient, such as in [7–9]. If PV power generation time series are available, this can be used to estimate PV metadata for

* Corresponding author.
E-mail address: david.lingfors@angstrom.uu.se (D. Lingfors).

https://doi.org/10.1016/j.solener.2025.113344
Received 23 October 2024; Received in revised form 14 January 2025; Accepted 10 February 2025
Available online 5 March 2025

individual systems. For instance, in [11] the tilt and azimuth where derived using a non-linear solver, fitting the measured and simulated PV power output during periods of clear-sky. The mean deviation between the normal vector of the actual and modelled PV system orientation was 4°. However, access to PV power time series is limited in most cases. In current PV system databases, the location of the PV system is often reported to be within the premises of a property [14]. On the other hand, recent AI models can identify the exact locations of PV systems in aerial images [10,12,15–21]. This makes it possible to derive the orientation from existing 3D models [12], through photogrammetry or LiDAR data [22–25]. Thus, finding the individual orientations enables more sophisticated analysis on local level, such as improved PV power forecasts [26,27], and hosting capacity studies [2,6,28], which are important from, e.g., aggregators' and grid operators' perspective, as PV penetration quickly increases. Aerial LiDAR data have been used extensively to map the rooftop solar energy potential globally [29]. Since distributed PV and ST systems most often are installed flush to the building's roof, LiDAR data are in most cases suitable for deriving the tilt and azimuth of existing SES, identified in aerial images. In some cases, however, LiDAR data are insufficient or non-representative of the SES orientation, e.g., when the SES is mounted on a stand, either on the roof or the ground. The aim of the study presented here, was to develop a method that estimates the azimuth and tilt satisfactorily, for SES of various configurations, across large spatial areas, such as municipalities.

The paper is structured as follows. In Section 2, the data used in the study are described. In Section 3, the proposed methodology for deriving the orientation of SES is presented. In Section 4, the results of the study are put forward and discussed in depth in Section 5. Finally, some conclusions can be found in Section 6.

2. Data

In this section, the raw datasets and how they were processed for the purpose of this study are presented. The data cover the three Swedish municipalities; Falun (60 000 inhabitants), Knivsta (21 000 inhabitants) and Uppvidinge (9 000 inhabitants).

2.1. Geospatial data

The Swedish Land Survey provides building footprint data within the 'GSD-Property Map' [30], which were used to identify building applied SES, including its orientation. Each building was also categorized in terms of its general purpose (e.g., residential) and detailed purpose (e.g., small house, detached). In addition, information about the property purpose was acquired from the Swedish Tax Agency. Different predefined combinations of the 7 general building purposes, the 49 specific building purposes and the 8 property purposes in Sweden were used to determine which type of general building category (or market segments) the SES belongs to, using the methodology and definitions described in [17]. Those are (1) Domestic residential houses (i.e., single-family houses), (2) Multi-family residential buildings, (3) Agricultural buildings, (4) Commercial buildings, (5) Industrial buildings, and (6) Public buildings.

LiDAR data, also provided by the Swedish Land Survey [31], where used to find the tilt and azimuth of building applied SES. The LiDAR dataset covers all of Sweden and is of relatively low resolution (1–2 pts/m^2), compared to LiDAR datasets covering a specific (often urban) area (see e.g., [32,33]). The year of the LiDAR surveys varied between and even within the three municipalities, where the oldest data were from 2018. Updates follow a 7-year cycle according to the Swedish Land Survey. The LiDAR data are classed as low point (noise), high point (noise), water, bridges, unclassified and ground in line with the standard protocol for LiDAR data [34], but only the two latter are used here; *unclassified* to find the SES orientation and *ground* for determining the building altitudes. *Unclassified* points where reclassified or discarded as described in [35], most importantly, points falling within building footprints where reclassified as *building*. In turn, building point outliers were discarded following the procedure described in [36]. In addition, building points less than <1 m above ground were considered noise in this study and discarded, as such points in some cases impacted the regression analysis to find the tilt negatively.

The Swedish Land Survey also provides aerial images in both raw format and as orthophotos, from which SES were identified using a machine learning method based on convolution neural networks (CNNs) (see Section 2.2). Each orthophoto cover 2.5 × 2.5 km, which corresponds to 15 625 × 15 625 pixels, i.e., an original resolution of 0.16 m/pixel.

2.2. Solar energy system ground truth

The dataset of SES was created using a machine learning model based on CNN, that was initially developed at Stanford [18], further developed in Germany [12,15], and trained and adapted for Swedish conditions in [17] (see the latter for details). The model annotates image tiles from the larger orthophotos (which are 17.25 x 17.25 m) as positive, if they contain a SES. However, the model does not include segmentation of the SES into polygons, which is possible for some other models, such as [16]. Polygons for true positives were created manually, and sometimes checked through visits, if visually inspecting the orthophotos was considered insufficient. During the manual checks, which included cross-checking with the databases of the local Distribution System Operators, 73 vertical systems were also discovered and added to the dataset for completeness. Also, bi-directional SES were also annotated. The CNN model was applied on orthophotos for the three municipalities; from 2022 for Falun (2 173 systems) and Uppvidinge (791 systems) and from 2021 for Knivsta (707 systems). New aerial images over Sweden are collected, following a 2-year cycle, according to the Swedish Land Survey.

3. Methodology

Section 3.1 describes how the tilt, azimuth, and position in space are derived for the SES, based on LiDAR data. Methods for handling six special cases, in which LiDAR data cannot be used for this, are presented in Section 3.2.

3.1. Orientation and position correction from LiDAR data

The orientation (tilt and azimuth) of a SES can be estimated by using LiDAR data, as the LiDAR dataset makes up a point cloud of xyz-coordinates. The orthogonal projection for the orthophotos is performed with respect to terrain elevation, but the heights of the buildings are not taken into account, which means that the roofs (and SES) are not in the correct position (if not exactly at nadir of the camera when the photo is taken). Consequently, if LiDAR data are to be used to derive the orientation of the SES, the polygon representing the identified SES needs to be aligned to the LiDAR data. Therefore, an *orthorectificaton* procedure was developed for aligning the SES polygon and the LiDAR data, illustrated stepwise in Fig. 1(a–j). The starting point is shown in Fig. 1(a), where a SES (in blue) has been identified, according to the method in [17], and (manually) segmented in the orthophoto. Here, the extent of the building, as it appears in the property map (dotted lines) and in the orthophoto (solid lines), including the roof ridge (dashed line), are marked. From Fig. 1(a) it is obvious that the building in the orthophoto is not orthogonal, i.e., the building was not at nadir of the airborne vessel when the aerial image was taken. If the SES is tagged as vertical or bi-directional, it is treated as a special case, as described in Section 3.2.

If neither tagged as vertical nor bi-directional, we next need to determine if the SES is ground-mounted or building applied, and, in the latter case, what buildings that should be considered. Since in some

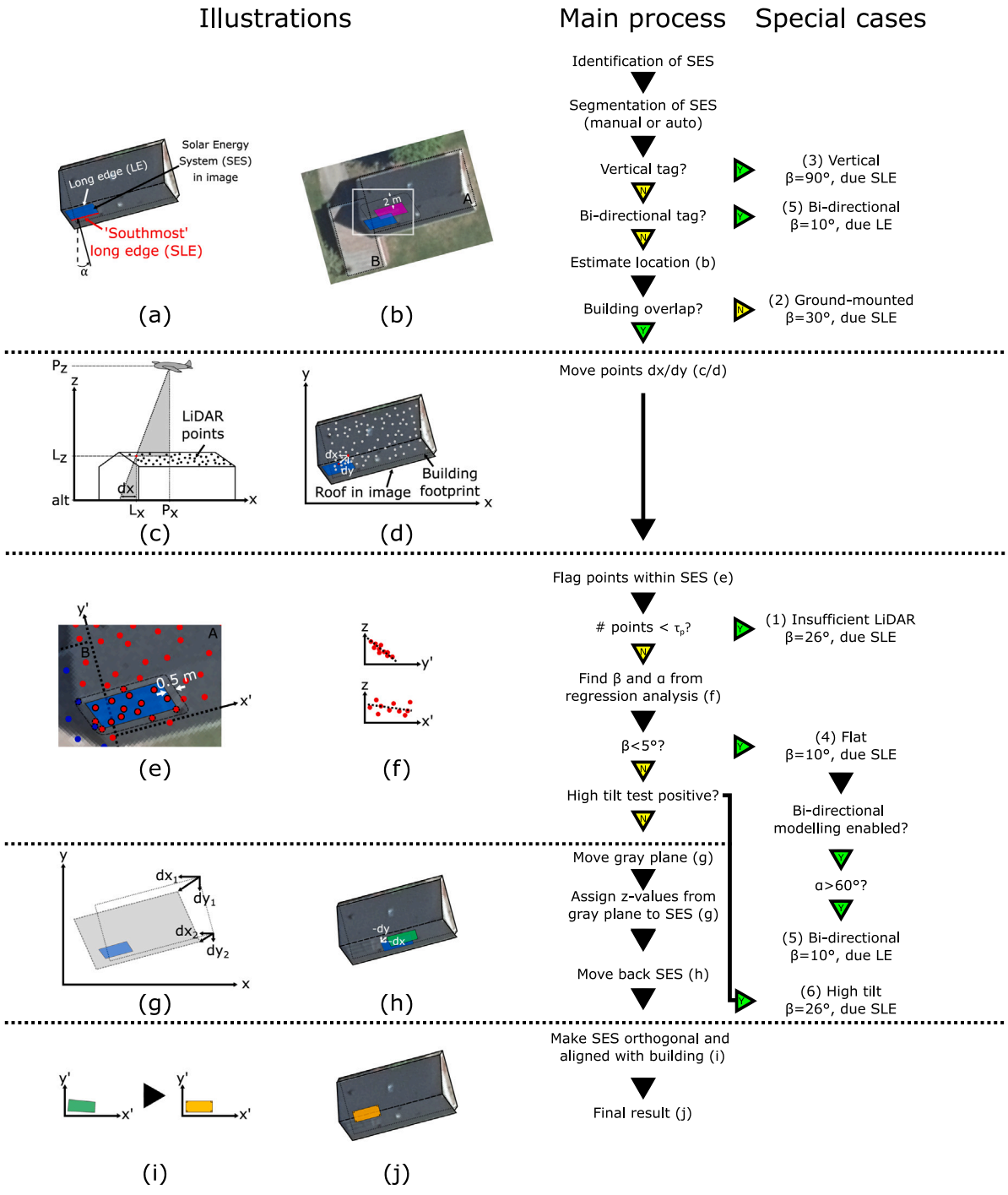

Fig. 1. Overview of the methodology to estimate the tilt and azimuth (α) of SESs identified in orthophotos (see text for details). The SES (initially blue) changes colour when its position and/or shape change. (For interpretation of the references to colour in this figure legend, the reader is referred to the web version of this article.)

cases, a ground-mounted SES in the orthophoto overlaps a building footprint and in other cases a building-applied SES is not overlapping a building at all, the SES is moved to roughly its actual position (purple in Fig. 1(b)), by assuming an altitude above ground (here set to 4.26 m, based on the mean of the roof eave of a sample of 100 buildings). The distance it should be moved is decided by the position of the SES in relation to the airborne vessel from which the aerial image was taken. This error in position along the x-axis, dx (and similarly dy along the y-axis), can be calculated as;

$$dx = L_z \frac{L_x - P_x}{P_z - L_z}, \quad (1)$$

where L and P denotes the coordinates of the LiDAR point(s) to be moved and the airplane's position, respectively. Here, z-values are relative to ground, which is estimated as a mean of ground-classified LiDAR points within 10 m of the studied building (or if < 5 LiDAR points, the radius is doubled to 20 m). This procedure is illustrated in Fig. 1(c), in which a LiDAR point (in red) is used as an example. Since the height of the SES was estimated, and therefore the movement was not exactly correct, it was found that buildings within a distance of 2 m from the moved SES are reasonable to consider as a trade-off between (1) not missing SES on high-rise buildings, and more importantly (2) not consider actual ground-mounted SES as building applied, and then falsely assuming a lack of LiDAR data (see below on how SES with

insufficient LiDAR data are treated). Following this logic, in Fig. 1(b) building A and B are considered. If there had been no buildings within 2 m, the SES would have been assumed to be ground-mounted, and a separate routine would have been used to estimate the orientation of it (see Section 3.2).

Next, LiDAR points falling within the building footprint, i.e., representing the morphology of the roof, and assumingly also the SES, are moved dx, and dy (according to Eq. (1)), respectively, as illustrated by the red point in Fig. 1(d), corresponding to the displacement of the roof/SES in the orthophoto. Note that for the illustrative example of Fig. 1, both dx and dy are negative, since the airplane was located northeast of the buildings, when the aerial image was taken.

Now, consider Fig. 1(e), which is a zoom-in of the example buildings, corresponding to the white box in Fig. 1(b). Here, red and blue LiDAR points have been moved, representing house A, and B, respectively. LiDAR points falling within the SES polygon are marked with a solid rim and are used to find the tilt of the SES, through linear regression (using Matlab's® *robustfit* function), in both the x'z- and the y'z-coordinate systems of the building (see Fig. 1(e) and (f)). The linear regression is not evaluated on the R2, but on the *z-error*, z_e, which is similar to the mean absolute error (MAE) and defined as [37]:

$$z_e = \frac{\sum |Z_m - Z_d|}{N_p}, \tag{2}$$

where Z_m and Z_d are the z-values for the linear model and the data, respectively, and N_p is the number of LiDAR data points. The reason for not considering the square of the errors is to not place too much weight on outliers [37].

If there are <10 LiDAR points within the SES polygon, points within 0.5 m from the SES are also included in the linear regression (see points with dashed rim in Fig. 1(e)). Since the position of the SES polygon is uncertain, the 0.5 m was deemed reasonable, as using a wider buffer increases the risk of including LiDAR points, e.g., representing bay windows or neighbouring buildings (e.g., for the latter, see the two blue points with dashed rim in Fig. 1(e)).

The plane, in which the SES lies, is now identified, but to consider the integrity of the shape of the SES, two steps, illustrated in Fig. 1(g) and h, are made. The (gray) plane in Fig. 1(g) is moved, following Eq. (1), i.e., it is moved in the same manner as the SES is dislocated from its actual position in the aerial image. Following Eq. (1), we have that $z_1/z_2 = dx_1/dx_2 = dy_1/dy_2$, and since $z_1 > z_2$ in Fig. 1(g), $dx_1 > dx_2$ and $dy_1 > dy_2$.

Then, z-coordinates from this moved (gray) plane are projected onto the (blue) SES, which is moved back in the other direction $(-dx, -dy)$, following Eq. (1), to its final position (green), which should correspond to its correct position in the xyz-space (see Fig. 1(h)). Finally, the SES polygon is aligned with the building and adjusted so that the corners are orthogonal (see Fig. 1(i)), giving the final position and shape of the (yellow) SES as illustrated in Fig. 1(j).

3.2. Special cases

There are a few special cases, in which the LiDAR cannot be used as basis for the orientation estimation. Firstly, the number of LiDAR points may be insufficient for the regression analysis (as illustrated in Fig. 1(f)). Thus, if the number of LiDAR points were $<\tau_p$, no regression analysis was performed (see Section 4.1.1 for the derivation of the optimal threshold τ_p). Instead, the tilt was set to 26° (based on the mean of a sample of 100 SES with a correctly identified azimuth). The azimuth was then derived from the normal of the *SLE* of the bounding box of the SES (see Fig. 1(a) for a definition of the SLE and the azimuth, α).

In a second case, when the SES is located >2 m from any building, it is assumed to be ground-mounted. In this case, the SES is assumed to have a tilt of 30°, and the azimuth based on the SLE of its bounding box (similar to Fig. 1(a)) and mounted so that the lower edge of the panels are 0.75 m above ground, which is common for ground-mounted systems [38]. Vertical systems could not be identified from the aerial images, but where added manually to make a complete dataset, making up the third special case. Similar to the two previous cases, SLE determines the azimuth, but the tilt was naturally set to 90°.

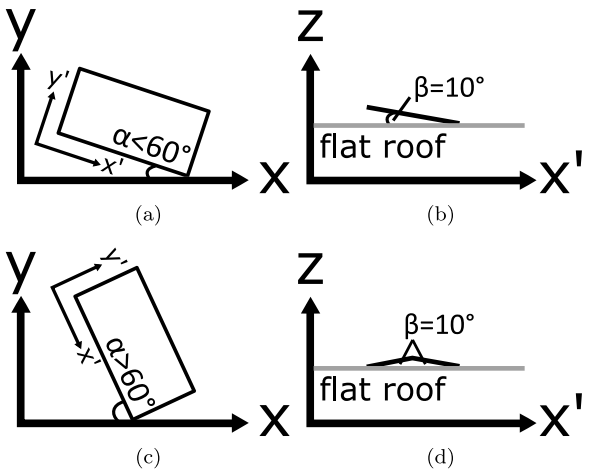

Fig. 2. Illustration of assumptions made for SES on flat roofs, where (a) and (b) represent single-directional SES (special case 4), and (c) and (d), bi-directional SES (special case 5), here with a threshold azimuth $\alpha > 60°$.

In a fourth case, when the tilt from the regression analysis is found to be <5°, the SES is assumed to be installed on a flat roof. The tilt is adjusted to 10°, since it is common practice to mount the SES with a tilt to get higher energy yield and less dust (and in Nordic climates also snow) accumulation [39]. However, the modelled azimuth on a flat roof is probably random. Therefore, as in the two previous cases, the azimuth is set in the direction of the SLE of the SES bounding box.

However, when the SLE is faced close to east or west on a flat roof, it is a good chance that the SES is actually bi-directional. Therefore, as a fifth case, the SES polygon is split into two, becoming bi-directional, as illustrated in Fig. 2(d). This split was either done automatically if $|\alpha| > 60°$ on a flat roof, but SES were also tagged manually as bi-directional. Both methods are evaluated in Section 4.2.1.

Sometimes the regression model outputs high tilts of a SES, mainly due to non-representative LiDAR data (i.e., the building was constructed after the LiDAR survey or facade or ground points were unintentionally included). Therefore, as a final sixth special case, for SES with derived high tilts and high z-errors, the LiDAR points were considered non-representative, and the SES was treated in the same way as in the first special case. More details on this is provided in Section 4.1.4.

4. Results

In this chapter, the results of the study are put forward. Section 4.1 presents the results of the model tuning, while in Section 4.2 the overall results are outlined for the three municipalities and different types of buildings.

4.1. Tuning of the model

This section presents the results from the tuning of the model, specifically highlighting the assumptions made for key parameters that yielded the highest model accuracy. These results were validated against a manually created ground truth, based on azimuth measurements performed in QGIS, supplemented by occasional on-site visual inspections. Furthermore, in Section 4.1.4, the model's ability to find a representative tilt is explored. The tuning of the model parameters was performed on the Falun dataset only, consisting of 2 173 systems.

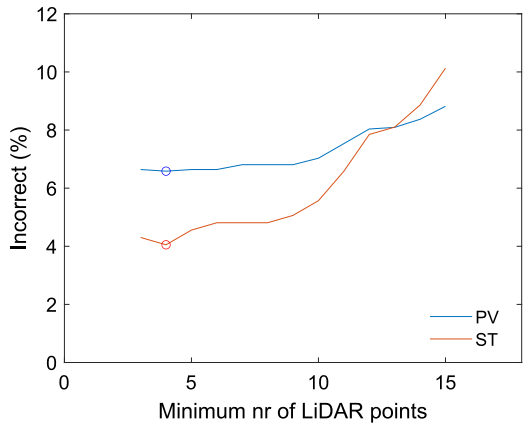

Fig. 3. Incorrectly modelled azimuths (in %) for PV and ST systems in Falun as function of the minimum LiDAR point threshold. (For interpretation of the references to colour in this figure legend, the reader is referred to the web version of this article.)

Fig. 4. Four SES polygons, where red lines marks the SLE and blue lines the SE if not equal to the SLE, for the 219 SES polygons that was found to have insufficient number of LiDAR points (<4), i.e., belonging to either the first or the sixth special case. (For interpretation of the references to colour in this figure legend, the reader is referred to the web version of this article.)

4.1.1. Minimum LiDAR point threshold

Including very few LiDAR points to find the tilt and azimuth of the SES through regression analysis, may result in poor model performance. Therefore different minimum LiDAR point thresholds (τ_p) where tested, and foremost validated against the azimuth ground truth. Fig. 3 shows similar precision in modelling the azimuth if 3–9 points where chosen as a minimum threshold, with best performance for four points (marked with circles). However, the accuracy for modelling the tilt may be low when using so few points, which is further explored in Section 4.1.4.

4.1.2. Southmost long edge assumption

In cases of insufficient LiDAR points within the SES, i.e., special case 1, the southmost long edge (SLE) was assumed to be the lower edge of the SES, and consequently the normal of that edge determining the azimuth (see red lines in Fig. 4). However, assuming that the SE is the lower edge, irrespective of being the longest or not, could also be a valid assumption, and was therefore tested. In Fig. 4, red lines mark the SLE, and blue lines the SE, if not being the same as the SLE. In this example, the SE assumption gives the correct azimuth for system b, while the SLE assumption should be used for system d. For systems a and c, the SLE and SE is the same. In cases when SLE and SE are not the same (blue in Fig. 4), the SLE assumption was favourable for 47 polygons out of total 71 polygons that was found to fall under special case 1 for the Falun dataset. In 10 cases, the azimuth was more towards north than south ($|\alpha| > 90°$), i.e., neither the SLE, nor the SE assumption was valid. To conclude, the SLE assumption gave the best model results overall.

Fig. 5. Examples of when aligning the SES to the building is not appropriate, to the left due to a mounting stand towards south and to the right due to a complex building. (For interpretation of the references to colour in this figure legend, the reader is referred to the web version of this article.)

4.1.3. Maximum rotation for building alignment

In the final step of the proposed method, illustrated in Fig. 1(i), the SES is rotated to align with the building. However, sometimes the SES is in fact not aligned with the building. Thus, a maximum rotation angle was sought to find a balance between aligning those that should be aligned, but at the same time avoid aligning those that should not. Examples of two cases in which the SES should not be aligned are illustrated in Fig. 5. To the left, the SES is mounted on a stand towards south, with a ~15° difference in azimuth compared to the building. To the right, the building is complex, making it hard to find its main orientation and therefore alignment should not be done. A sensitivity analysis of the maximum rotation angle was performed for 3° – 15°, and 6° was found to provide the best model accuracy.

4.1.4. Evaluation of tilt accuracy

Determining the true value of the tilt is not straightforward, as it (unlike the azimuth) cannot be inferred by examining aerial images. Inspecting the z-error (z_e) and tilt as a function of the number of LiDAR points, as illustrated in Fig. 6, can give some guidance. In the figure, only SES with <100 LiDAR points used for the linear regression are included for better visibility. Red markers are for SES where the azimuth is incorrectly modelled, representing 2.5% of all SES in the figure. Fig. 6(a) shows that a high z-error is over-represented among incorrectly modelled SES, but it also illustrates that it would impact correctly modelled SES, if one would adjust the model to disqualify calculations resulting in high z-errors. However, a poor regression analysis, e.g., due to noise from trees (for buildings constructed after the LiDAR survey) or the facade, may also result in a high tilt. Fig. 6(b) shows that the tilt and z-error often are high at the same time. Overestimated tilts, will in turn result in overestimated SES area and energy yield and should be avoided. Therefore, SES with $r_A > 4$, where r_A is defined as the ratio between the modelled SES area and the area in the aerial image, or a SES with a tilt $\beta > 75°$, or SES fulfilling three criteria; (i) $\beta > 50°$, (ii) $z_e > 0.5$ and (iii) $r_A > 3$, were flagged. These systems were instead treated as if having insufficient LiDAR points. This removed the overestimated tilt of 8 SES, but more importantly corrected the active SES area of 1400 m^2, which represents 2% of the total in Falun. The azimuth modelling accuracy, although, remained unchanged when implementing this.

Fig. 7 is an histogram of the z-errors for all systems in Falun, with the 75th, 90th, 95th and 98th percentiles marked. From the figure we see that the z-error is small for most systems, for 75% of the them <0.0744 m. Fig. 8 illustrates what this means, in terms of the linear regression that determined the tilt for the four SES lying closest to each percentile marked in Fig. 7. There are outliers in all regressions but Fig. 8(c), in which the points are more scattered around the regression line instead. Since both the Matlab's® *robustfit* function give little weight to outliers [40], likewise the z-error metric (see Eq. (2)), the fit is seemingly good, even in Fig. 8(d), which has three distinct outliers (i.e., LiDAR noise on the facade).

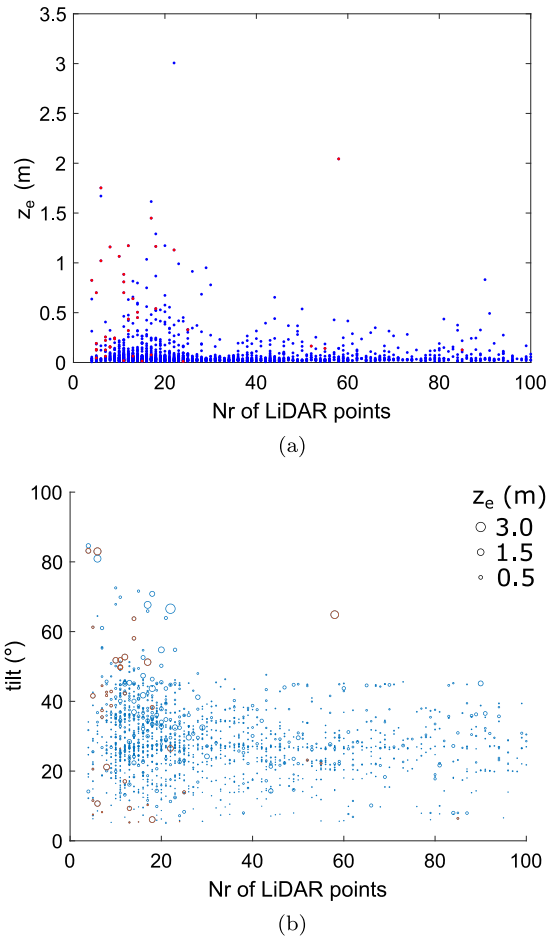

Fig. 6. z-error z_e (a) and tilt (b) as function of number of LiDAR points per SES, respectively. The size of the circles in (b) represents the magnitude of the z-error. Red markers indicate systems with erroneously modelled azimuths in both figures. (For interpretation of the references to colour in this figure legend, the reader is referred to the web version of this article.)

A sample of SES was also examined using Google street view, in which the tilt was measured on the screen when possible, i.e. not being obscured and viewed in profile. Out of 200 examined systems in Falun, the tilt of 39 SES could be confidently measured in this way, and for those the MAE was 3.6°.

4.2. Model results

In this section, the overall model results are outlined. In Section 4.2.1, the azimuth accuracy and the origins of model errors are discussed. Furthermore, in Section 4.2.2, the distribution of azimuths and tilts derived from the model are presented and analysed.

4.2.1. Azimuth accuracy and origins of errors

In Section 3.2, six special cases were presented, in which LiDAR data could not be used for different reasons to determine the tilt and azimuth of SES. These special cases, along with the ordinary case, i.e., the *regression model* illustrated in Fig. 1, are presented in Table 1 in terms of the accuracy of the azimuth modelling. The azimuth was deemed correct or True (T) if within 3°, and False (F) otherwise. A deviation within 3° is probably due to errors when manually determining the ground truth from the orthophotos. Table 1 also includes the accuracy (T/(T+F)) and MAE (°) for each case. For the MAE, only the incorrectly modelled SES were included, as an indication of how off the model was in those cases. As can be seen, if the azimuth is incorrect, it is often

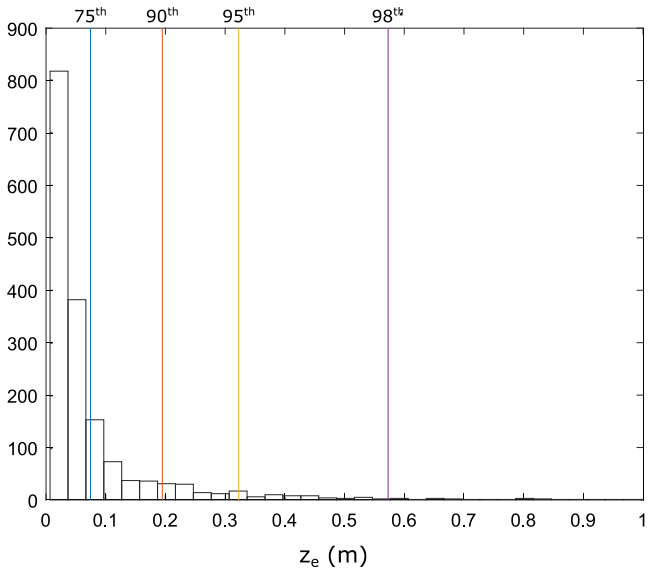

Fig. 7. Histogram of z-errors for SES in Falun with the 75th, 90th, 95th and 98th percentiles marked.

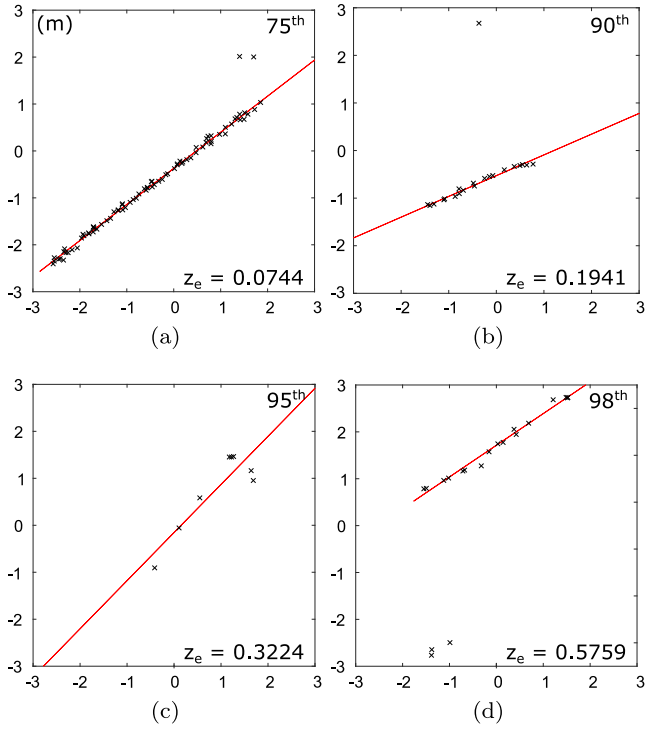

Fig. 8. Regression lines (red) for four systems with z-errors (z_e) representing the 75th, 90th, 95th and 98th percentiles, respectively, of all systems in Falun.

vastly incorrect, often around 90° (or sometimes even 180°, which gives an MAE > 90°), since the orientation of the building is used as reference. For SES classed as ground-mounted, the azimuth is actually correct in half (4) of the cases, but marked as false anyway, since they are actually building-applied. Furthermore, the model accuracy is expressed in two ways in the two bottom rows of Table 1. The difference between those two are discussed in the following.

First, it should be stressed that the proposed procedure for modelling some roofs as bi-directional (see Fig. 2) worsened the overall results compared to just treat them as flat, and was therefore

Table 1
Number of true (T) (if within 3° from the correct) and false (F) modelled azimuths for PV and ST systems, respectively, compared to the ground truth for the three municipalities (Falun, Knivsta and Uppvidinge), presented for the ordinary case using a regression model and for six special cases. For *Accuracy (Man)* vertical systems are included and bi-directional systems are manually annotated, hence, representing the numbers presented for each case and municipality. MAE (°) represents the error for the false modelled azimuths only. *Accuracy (Auto)* represents the case when vertical systems are excluded and all bi-directional systems are assumed to not have been identified.

Case	Falun				Knivsta				Uppvidinge				Total		Accuracy	MAE (°)
	PV		ST		PV		ST		PV		ST					
	T	F	T	F	T	F	T	F	T	F	T	F	T	F		
(0) Regression model	1322	35	351	11	481	6	71	2	294	35	33		2552	89	96.6%	92
(1) Insufficient LiDAR	148	39	17	4	10	3	3		12	5	1		191	51	78.9%	103
(2) Ground-mounted	15	3	1		28	3	2			2			46	8	85.2%	46
(3) Vertical	46				23				4				73	0	100.0%	–
(4) Flat	133	14	6	1	32	3	1		313	3			485	21	95.8%	113
(5) Bi-directional	17	2			39				87	1			143	3	97.9%	7
(6) High tilt	5		2	1					1				8	1	88.9%	93
Total	1686	93	377	17	613	15	77	2	711	46	34		3498	173		96
Accuracy (Man)	94.8%		95.7%		97.6%		97.5%		93.9%		100.0%		95.3%			
Accuracy (Auto)	*93.7%*		*95.7%*		*91.1%*		*97.5%*		*82.3%*		*97.1%*		*91.2%*			

Fig. 9. Two examples when LiDAR acquisition is poor due to black surfaces; to the left, the west-facing roof facet has very few (red) LiDAR recordings and to the right, there are few recordings within the (blue) SES polygon, which in this case is a solar thermal system. (For interpretation of the references to colour in this figure legend, the reader is referred to the web version of this article.)

Table 2
Categorized reasons for incorrectly modelled azimuths per technology.

Reason	PV	ST
Building polygon missing (not ground)	6	0
Not identified as ground-mounted	6	0
SLE not valid for bi-directional SES	3	0
SLE not valid when insufficient points	39	5
SLE not valid for ground system	2	0
SLE not valid for flat roof	50	1
Complex building	3	0
LiDAR noise	9	6
New building (after LiDAR survey)	13	0
Incorrectly oriented building polygon	3	3
Mounting stand	12	2
Bay window	5	2
Incorrect orthophoto	2	0
Mansard roof ->high tilt	1	0
Total SES (#)	3164	507
Total errors (#)	154	19
Total errors (%)	4.7	3.7

abandoned. Since vertical systems, and currently bi-directional, cannot be automatically identified in aerial images by machine learning approaches, *Accuracy (Auto)*, in Table 1, expresses the accuracy of the model (91.2%), if fully integrating an unsupervised automatic model that identifies SES in aerial images, i.e., excluding vertical systems and assuming that none of the bi-directional systems could be identified. On the other hand, the 146 bi-directional SES polygons in the three municipalities are located on only 8 large buildings. Manually annotating these systems are therefore a fairly simple step, increasing the overall model performance substantially. In the future a multi-class U-net model could perhaps be able to label different SES, such as regular or bi-directional systems. Therefore, *Accuracy (Man)* refers to the case when the bi-directional systems were manually annotated and vertical systems were included. This gave an overall accuracy of 95.3%.

Furthermore, Table 1 shows that the regression model is applicable in most cases (71.9%), with an accuracy of 96.6%. The lowest accuracy (78.9%) is found when there are insufficient LiDAR points, i.e., the first special case. There are different reasons for insufficient LiDAR points; if the LiDAR survey predates the construction of the building, there might be no non-ground LiDAR points, within the building, nor SES polygon. The LiDAR data acquisition may be poor due to black surfaces absorbing the light [41]. In this context, an absorbing black surface may be part of the roof, as illustrated in the left panel of Fig. 9. It may also be the SES itself, as illustrated in the right panel of Fig. 9. In these two examples, the azimuth and tilt were correctly modelled anyway, since neighbouring LiDAR points were included (see Fig. 1(e)), but in other examples we noticed an incorrectly modelled tilt, when linear regression was made with few points.

Table 2 lists the reasons for incorrectly modelled azimuths, clearly showing that assuming that the azimuth should be defined by southmost long edge (SLE) of the SES is not always valid, but the best assumption available, as discussed in Section 4.1.2. There are a number of other reasons that are less common; when the *building polygon is missing*, the SES is falsely treated as a ground-mounted system, and similarly, sometimes systems are *not identified as ground-mounted*, although they actually are installed on the ground, but within the 2 m threshold distance from a building (see Section 3.1), and therefore classified as building applied. However, the azimuth is in many cases correctly modelled for these systems anyway. *Complex building* means that it is difficult to determine the main orientation of the building (see right image in Fig. 5). *LiDAR noise* means that the LiDAR points (which often are few) do not represent the roof, but instead an overhanging tree, the facade, ground, a neighbouring building or simply unidentified, unfiltered noise. In some cases, the building polygon in the property map is *incorrectly oriented* relative to its correct position, which directly impacts the model output. The left image of Fig. 5 exemplifies another model error, which is when the SES is on a *mounting stand* that is not aligned with the building. Small extrusions or *bay windows*, sometimes result in a poor regression and incorrect azimuth. For one building (with two PV polygons), the orthorectification of the aerial image had an error, however, the issue of *incorrect orthophotos* is probably not that common. The last example is when a SES is located near the eave of a Mansard roof, which often has a high tilt (>60°). In many cases, LiDAR points would be insufficient, yet the SLE assumption is valid, but in areas where this type of roof is common, it may cause more problems.

4.2.2. Azimuth and tilt distributions

In Fig. 10, distributions of tilts derived through linear regression and ground truth azimuths are presented for all 3 671 SES in the three

Table 3
Best fitted probability density functions to the tilt distribution of each building category, including their corresponding coefficients for the Kolmogorov–Smirnov test (KS) and KS integrals (KSI), respectively. If h = 1, the null hypothesis is rejected at the 95% significance level. GEV stands for Generalized Extreme Value.

Market segment	Test	Dist. type (coeffs)	KS(I) score	h	coeff. 1	coeff. 2	coeff. 3	coeff. 4
Domestic	KS	GEV (k, σ, μ)	0.0697	1	−0.1627	9.2841	24.0469	
	KSI	Logistic (μ, σ)	0.8386°		27.7182	5.4594		
Multi-family	KS	Logistic	0.0888	0	23.9223	5.4309		
	KSI	Logistic	1.8197°		23.9223	5.4309		
Agricultural	KS	Stable (α, β, γ, δ)	0.0567	0	1.7468	−0.7867	5.7252	30.5548
	KSI	Stable	0.9549°		1.7468	−0.7867	5.7252	30.5548
Commercial	KS	Nakagami (μ, ω)	0.1210	0	2.2352	442.1891		
	KSI	Rayleigh (B)	1.5844°		14.8692			
Public	KS	Rayleigh	0.0799	0	13.0621			
	KSI	Logistic	1.5974°		15.9030	4.8652		
Industrial	KS	tLocationScale (μ, σ, ν)	0.1831	0	14.0976	4.5921	3.5660	
	KSI	tLocationScale	1.6433°		14.0976	4.5921	3.5660	

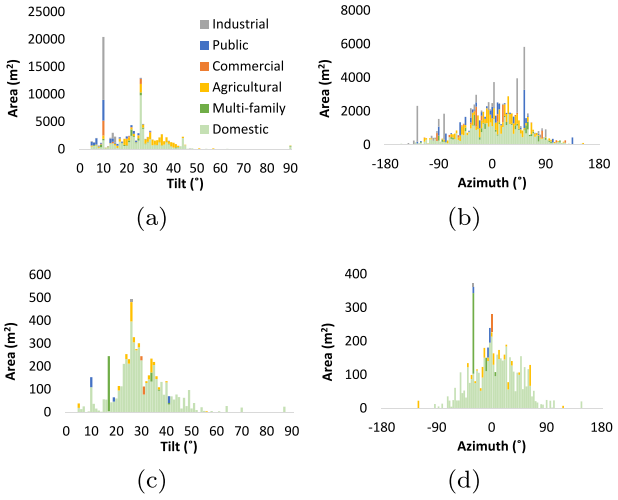

Fig. 10. Distribution of modelled tilts and ground truth azimuths from all PV (a and b) and ST systems (c and d) in the three municipalities, presented per building category and weighted on SES area. An azimuth of −90° represents East, 0° represents South, and 90° represents West. (For interpretation of the references to colour in this figure legend, the reader is referred to the web version of this article.)

municipalities. Fig. 10(a) and (b) represent PV systems and Fig. 10(c) and (d) represent ST systems. The bars are coloured according to the SES area of each building category, defined in Section 2.1. This means that large single SES may result in spikes in the histograms, such as at 18° in Fig. 10(c). Two clear spikes can be found in Fig. 10(a) and (c); one at 10°, representing flat roofs, of which industrial, public, and commercial buildings are over-represented. The other spike is at 26°, representing building-applied SES for which LiDAR data were insufficient for regression analysis (see special case 1 in Section 3.2).

Domestic residential houses dominate among ST systems and the azimuth distribution is more narrow than that of PV systems. One plausible reason is that the installation of ST systems took place before the roll-out of PV systems started in Sweden [17], as almost all currently existing ST systems were installed before 2011 when the subsidy program for ST systems was phased out. Consequently, all the best roofs for SES were unoccupied for the early ST market. In addition, since the heat generated by ST systems is typically stored in accumulator tanks, there is no need to match consumption and production to reach high self-consumption and ST systems therefore benefit from an optimal orientation to maximize economic feasibility. For PV systems without battery storage, it is reasonable and quite common to install them facing more towards the east or west. This orientation helps align the generation profile with both the load profile and the higher spot prices that typically occur in the mornings and evenings.

In Fig. 11, the distributions of tilts per building category, are presented, limited to PV systems with a correctly modelled azimuth through the regression analysis. The average tilt and sample size, N, are indicated in the upper right corner of each subplot. Distributions, included in the Matlab's® *fitdist* function, that best fits the distribution of modelled tilts, are included in each subplot. The best fitting distributions are determined by (i) the Kolmogorov–Smirnov (KS) test on the cumulative distribution functions (CDFs), and (ii) according to the KS test integral (KSI), which is defined as the area or deviation between the CDFs of the data and distribution function [42,43]. The best fitting distributions, including KS and KSI test scores and coefficients are presented in Table 3. Only for domestic residential houses could the null hypothesis (h in Table 3) at the 95% significance level be rejected. It should be noted that similar KS test scores where achieved for several distributions, and therefore 100 000 samples from the CDF were needed for the KS test to converge to one distribution. However, for public buildings (see Fig. 11(e)), this was not enough for converging, and the test scores were similar for the Rician and Weibull distributions. The low number of data points for all building categories, except for domestic residential houses, makes it difficult to conclude that these distributions are general, even for Sweden, but they were nonetheless included here as a reference.

5. Discussion

The first point of discussion relates to the tilt distribution results presented last in Section 4.2.2. The average tilt of 28° for single-family houses lies close to the assumption of 26° used for SES with insufficient LiDAR data, based on a sample of 100 correctly modelled azimuths (as described in Section 3.2). The area-weighted mean, if considering all building categories, is 26.8°, which means that the assumption holds if the building category is unknown. However, there are significant differences between the building categories, especially for industrial, public and commercial buildings where the average tilt was found to be significantly lower (15° – 20°) than for residential and agriculture buildings. This means that if the building category is known, the assumed tilt should be adapted to the building category (when linear regression is not possible), if a statistical representation of SES for different building segments across a region is sought.

Another observation made is that the accuracy of the LiDAR data relies on the number of new buildings (and ultimately potential SES) between the last LiDAR and aerial image surveys. If the built environment is developing fast in a certain region, the number of incorrectly modelled orientations due to *new building polygons* (since the LiDAR survey) would probably be greater. We saw this in Knivsta, which is one of the fastest growing and developing municipalities in Sweden, explained by its strategic location between Stockholm and Uppsala. This can be contrasted to Uppvidinge, a rural municipality far from larger cities, where there are very few new buildings erected.

We further noticed that the SES themselves may result in a poorer LiDAR point acquisition (see right panel of Fig. 9), probably since they are black, that may result in the wrong tilt and/or azimuth. This problem is mainly manifested for older systems, predating the latest

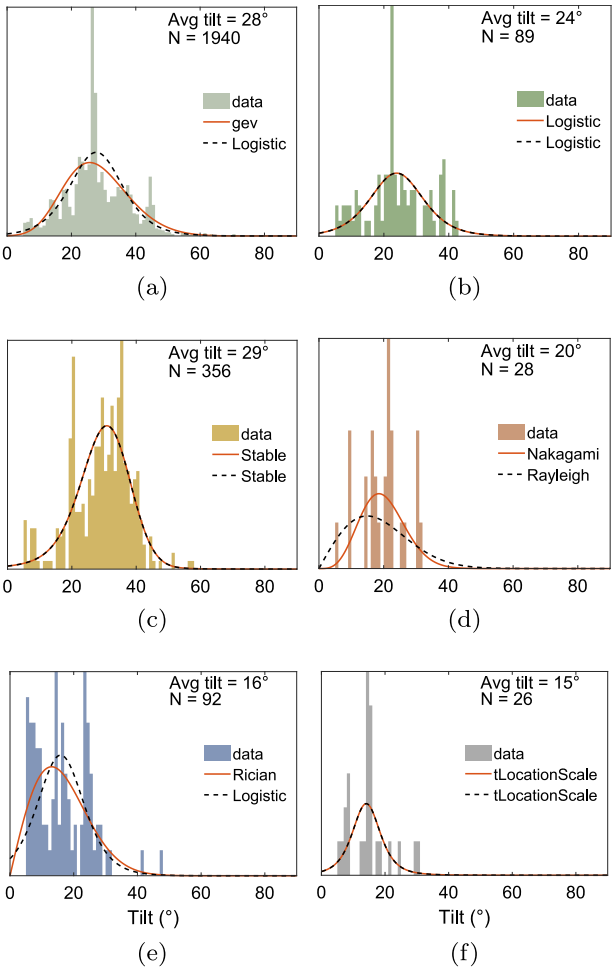

Fig. 11. Distribution of modelled tilts limited to buildings with correctly modelled azimuths through regression analysis. Subplots are per building category (a) domestic residential houses, (b) multi-family residential buildings, (c) agricultural buildings, (d) commercial buildings, (e) public buildings and (f) industrial buildings.

LiDAR survey, but this group of SES will grow each time a new LiDAR survey is done, and is probably already substantial in more mature PV markets than the Swedish. Using LiDAR data that predate the SES installation may be one way around it (given that the installation date is known or can be determined), or if possible, combining multiple LiDAR surveys to increase point density. However, the latter comes with the risk that changes in the built environment may have happen between the surveys.

As discussed in Section 1, in several previous studies, more or less incomplete databases of tilts and azimuths are used for simulating wide-area PV power output. Ref. [4] showed that the reported azimuth was incremental in many cases, e.g., reported as south, southeast, east, etc, and in [13], the orientation of nearby systems were used to interpolate to the PV systems of unknown orientation. While such approaches may be adequate for broad regional studies, more precise metadata on PV systems may be crucial at a local level. This information can assist local grid operators in grid planning (e.g., investments in grid reinforcement) and operational management (e.g., implementing measures to mitigate grid constraints caused by high local power generation). In combination with automatic detection [17], and segmentation of PV systems [16], the derived LiDAR method in this study could potentially provide grid operators with accurate and up-to-date metadata about current PV systems in the local grids. In addition to grid operators, aggregators or actors monitoring the performance of the PV system, may need access to metadata for accurate forecasts or for identifying malfunctions. Once the LiDAR data have been processed, the method quickly (within minutes) finds the tilts and azimuths of all SES across a municipality, and could thus be a valuable tool for these actors.

In [12] a similar methodological framework is presented, called the *3D-PV-Locator*, with the difference from this study that the orientation is derived from existing CityGML-based 3D city models [44]. The ground truth used to evaluate the performance of the *3D-PV-Locator* is based on the German PV registry, where azimuths are reported in 45° bins (compared to 3° in this study). In 63% of cases, the azimuth is modelled correctly in the *3D-PV-Locator* (compared to 91%–95% in this study). However, the authors acknowledge the reliability issues of self-reported metadata in the German PV registry. Consequently, their model may perform better or worse, and field visits – such as those conducted in this study – would have provided a more accurate ground truth and, in turn, a more reliable model evaluation.

In [25], a smaller, but quality-controlled, set of ground truth data was used, as it had been utilized in other research projects. By applying a Hough transform to determine the azimuth angle, they achieved an accuracy of 80%. In contrast, our study demonstrates a higher accuracy in modelling the azimuth (91%–95%). However, it should be noted that the segmentation step in our study was performed manually – a time-consuming process that is ideally avoided – which likely contributed to the improved overall accuracy.

While accurate 3D models may very well be used to determine the orientation of existing SES, they mainly exist for urban areas, due to mutual benefits and cost-efficiency of producing them in densely built environments. In rural areas, on the other hand, such 3D models cannot be justified and it is in rural areas the primary impact of distributed PV on the local power grid often occurs [6,45,46]. Due to the radial structure of the grid, long distances, and the relatively few customers served by each substation, the addition of each new PV system can significantly affect power quality in rural grids. This can lead to violations of the grid's hosting capacity, commonly manifested as voltage rises during sunny days when power generation is high and demand is low. Thus, the approach presented here, using low-resolution LiDAR data, provides a viable option to accurately estimate the orientation of SES, which in turn can be used as input to grid operation and planning.

6. Conclusions

In this paper, a method is proposed to find the orientation (i.e., tilt and azimuth) of SES from LiDAR data. The method orthorectifies the polygons, representing the SES in aerial images, to match the LiDAR data on which linear regression is used to find the orientation. Furthermore, the method handles six special cases where linear regression is not feasible; (1) insufficient number of LiDAR points, (2) ground-mounted systems, (3) vertical systems, (4) systems on flat roofs, that (5) may be bi-directional, and (6) systems with abnormally high tilt and poor regression metrics. The method was evaluated mainly with respect to the ground truth of the azimuth for 3 671 SES in three Swedish municipalities, which were identified from aerial images using CNN. The azimuth was correctly modelled for 91%–95% of the systems. It was also found that the distribution of azimuths was more narrow for ST systems than for PV systems. A manually derived ground truth of the tilt for 39 systems gave a mean absolute error of 3.6°. Combining with a qualitative assessment of samples, representing different percentiles of the MAE (or z-error) for the linear regression model that was used to find the tilts, indicated that the model performs well.

In contrast to previous studies, the method proposed here – combined with recent advances in developing machine learning approaches that identify and segment SES in aerial images – could provide grid operators with more precise tilts and azimuths with respect to the installed PV systems in the local grid. Thus, the method is believed to enable more accurate PV power simulations and forecasts, and in turn, improved grid operation and planning.

CRediT authorship contribution statement

David Lingfors: Writing – original draft, Visualization, Validation, Software, Methodology, Investigation, Formal analysis, Data curation, Conceptualization. **Robert Johansson:** Writing – review & editing, Validation, Software, Methodology, Investigation, Data curation. **Johan Lindahl:** Writing – review & editing, Visualization, Validation, Resources, Project administration, Methodology, Investigation, Funding acquisition, Formal analysis, Data curation, Conceptualization.

Declaration of competing interest

The authors declare that they have no known competing financial interests or personal relationships that could have appeared to influence the work reported in this paper.

Acknowledgements

This work was supported by the Swedish Energy Agency, Sweden [P2023-00440], and forms part of the Swedish strategic research programme StandUp for Energy.

References

[1] G. Masson, M. de l'Epine, I. Kaizuka, Trends in Photovoltaic Applications 2023, Technical Report, 2024, pp. 1–96, URL: www.iea-pvps.org.

[2] S.M. Ismael, S.H. Abdel Aleem, A.Y. Abdelaziz, A.F. Zobaa, State-of-the-art of hosting capacity in modern power systems with distributed generation, Renew. Energy 130 (2019) 1002–1020, http://dx.doi.org/10.1016/j.renene.2018.07.008.

[3] R. Luthander, J. Widén, J. Munkhammar, D. Lingfors, Self-consumption enhancement and peak shaving of residential photovoltaics using storage and curtailment, Energy 112 (2016) 221–231, http://dx.doi.org/10.1016/j.energy.2016.06.039.

[4] S. Killinger, D. Lingfors, Y.-M. Saint-Drenan, P. Moraitis, W. van Sark, J. Taylor, N.A. Engerer, J.M. Bright, On the search for representative characteristics of PV systems: Data collection and analysis of PV system azimuth, tilt, capacity, yield and shading, Sol. Energy 173 (August) (2018) 1087–1106, http://dx.doi.org/10.1016/j.solener.2018.08.051, URL: https://linkinghub.elsevier.com/retrieve/pii/S0038092X18308211.

[5] D. Lingfors, J. Widén, Development and validation of a wide-area model of hourly aggregate solar power generation, Energy 102 (2016) 559–566, http://dx.doi.org/10.1016/j.energy.2016.02.085, URL: http://www.sciencedirect.com/science/article/pii/S0360544216301475 https://doi.org/10.1016/j.energy.2016.02.085.

[6] E. Hartvigsson, M. Odenberger, P. Chen, E. Nyholm, Estimating national and local low-voltage grid capacity for residential solar photovoltaic in Sweden, UK and Germany, Renew. Energy 171 (2021) 915–926, http://dx.doi.org/10.1016/j.renene.2021.02.073.

[7] M. Pierro, F.R. Liolli, D. Gentili, M. Petitta, R. Perez, D. Moser, C. Cornaro, Impact of PV/Wind forecast accuracy and national transmission grid reinforcement on the Italian electric system, Energies 15 (23) (2022) http://dx.doi.org/10.3390/en15239086.

[8] Y.M. Saint-Drenan, G.H. Good, M. Braun, T. Freisinger, Analysis of the uncertainty in the estimates of regional PV power generation evaluated with the upscaling method, Sol. Energy 135 (2016) 536–550, http://dx.doi.org/10.1016/j.solener.2016.05.052.

[9] U.H. Ramadhani, D. Lingfors, J. Munkhammar, J. Widén, On the properties of residential rooftop azimuth and tilt uncertainties for photovoltaic power generation modeling and hosting capacity analysis, Sol. Energy Adv. 3 (February) (2023) 100036, http://dx.doi.org/10.1016/j.seja.2023.100036.

[10] M. Zech, J. Ranalli, Predicting PV areas in aerial images with deep learning, Conf. Rec. IEEE Photovolt. Spec. Conf. 2020-June (2020) 0767–0774, http://dx.doi.org/10.1109/PVSC45281.2020.9300636.

[11] S. Killinger, N. Engerer, B. Müller, QCPV: A quality control algorithm for distributed photovoltaic array power output, Sol. Energy 143 (2017) 120–131, http://dx.doi.org/10.1016/j.solener.2016.12.053, URL: http://linkinghub.elsevier.com/retrieve/pii/S0038092X16306600.

[12] K. Mayer, B. Rausch, M.L. Arlt, G. Gust, Z. Wang, D. Neumann, R. Rajagopal, 3D-PV-locator: Large-scale detection of rooftop-mounted photovoltaic systems in 3D, Appl. Energy 310 (November 2021) (2022) 118469, http://dx.doi.org/10.1016/j.apenergy.2021.118469.

[13] G. Kasmi, L. Dubus, P. Blanc, Y.M. Saint-Drenan, Towards unsupervised assessment with open-source data of the accuracy of deep learning-based distributed PV mapping, CEUR Work. Proc. 3343 (2022).

[14] IEA-PVPS, Data Model for PV Systems, Technical Report, IEA-PVPS, 2020.

[15] K. Mayer, Z. Wang, M.L. Arlt, D. Neumann, R. Rajagopal, DeepSolar for Germany: A deep learning framework for PV system mapping from aerial imagery, in: SEST 2020 - 3rd International Conference on Smart Energy Systems and Technologies, 2020, http://dx.doi.org/10.1109/SEST48500.2020.9203258.

[16] A. Frimane, R. Johansson, J. Munkhammar, D. Lingfors, J. Lindahl, Identifying small decentralized solar systems in aerial images using deep learning, Sol. Energy 262 (July) (2023) 111822, http://dx.doi.org/10.1016/j.solener.2023.111822.

[17] J. Lindahl, R. Johansson, D. Lingfors, Mapping of decentralised photovoltaic and solar thermal systems by remote sensing aerial imagery and deep machine learning for statistic generation, Energy AI 14 (2023) 19, http://dx.doi.org/10.1016/j.egyai.2023.100300, URL: https://linkinghub.elsevier.com/retrieve/pii/S2666546823000721.

[18] J. Yu, Z. Wang, A. Majumdar, R. Rajagopal, DeepSolar: A machine learning framework to efficiently construct a solar deployment database in the United States, Joule 2 (12) (2018) 2605–2617, http://dx.doi.org/10.1016/j.joule.2018.11.021.

[19] B.B. Kausika, D. Nijmeijer, I. Reimerink, P. Brouwer, V. Liem, Geoai for detection of solar photovoltaic installations in the Netherlands, Energy AI 6 (August) (2021) 100111, http://dx.doi.org/10.1016/j.egyai.2021.100111.

[20] Z. Guo, J. Lu, Q. Chen, Z. Liu, C. Song, H. Tan, H. Zhang, J. Yan, TransPV: Refining photovoltaic panel detection accuracy through a vision transformer-based deep learning model, Appl. Energy 355 (November 2023) (2024) 122282, http://dx.doi.org/10.1016/j.apenergy.2023.122282.

[21] H. Tan, Z. Guo, Z. Lin, Y. Chen, D. Huang, W. Yuan, H. Zhang, J. Yan, General generative AI-based image augmentation method for robust rooftop PV segmentation, Appl. Energy 368 (February) (2024) 123554, http://dx.doi.org/10.1016/j.apenergy.2024.123554, URL: https://linkinghub.elsevier.com/retrieve/pii/S0306261924009371.

[22] R. Wang, 3D building modeling using images and LiDAR: a review, Int. J. Image Data Fusion 4 (4) (2013) 273–292, http://dx.doi.org/10.1080/19479832.2013.811124, URL: http://www.tandfonline.com/doi/abs/10.1080/19479832.2013.811124.

[23] D. Lingfors, S. Killinger, N.A. Engerer, J. Widén, J.M. Bright, Identification of PV system shading using a LiDAR-based solar resource assessment model: an evaluation and cross-validation, Sol. Energy 159 (2018) 157–172, http://dx.doi.org/10.1016/j.solener.2017.10.061.

[24] D. Lingfors, J. Widén, Evaluation of datasets and methods to derive 3D building models and their influence on PV power integration studies, in: Solar Integration Workshop Stockholm 2018, Energynautics GmbH, Stockholm, 2018.

[25] A.S. Edun, K. Perry, J.B. Harley, C. Deline, Unsupervised azimuth estimation of solar arrays in low-resolution satellite imagery through semantic segmentation and hough transform, Appl. Energy 298 (March) (2021) 117273, http://dx.doi.org/10.1016/j.apenergy.2021.117273.

[26] C.F. Coimbra, J. Kleissl, Overview of solar-forecasting methods and a metric for accuracy evaluation, in: J. Kleissl (Ed.), Solar Energy Forecasting and Resource Assessment, first ed., Academic Press, Boston, 2013, pp. 171–194, (Chapter 8).

[27] M. Pierro, D. Moser, C. Cornaro, Machine learning-based PV power forecasting methods for electrical grid management and energy trading, Machine Learning and Data Science in the Power Generation Industry: Best Practices, Tools, and Case Studies, Elsevier Inc., 2021, pp. 165–194, http://dx.doi.org/10.1016/B978-0-12-819742-4.00008-1.

[28] D. Lingfors, J. Munkhammar, J. Lindahl, Solar resource-efficiency gain for energy communities based on current solar energy system deployment, in: ECEEE 2024 Summer Study Proceedings: Sustainable, Safe & Secure Through Demand Reduction, ECEEE, 2024, pp. 575–583.

[29] S. Freitas, C. Catita, P. Redweik, M. Brito, Modelling solar potential in the urban environment: State-of-the-art review, Renew. Sustain. Energy Rev. 41 (2015) 915–931, http://dx.doi.org/10.1016/j.rser.2014.08.060, URL: http://www.sciencedirect.com/science/article/pii/S1364032114007461.

[30] Swedish Land Survey, Product Description: GSD-Property Map, Vector, Technical Report, Swedish Land Survey, Gävle, 2018, URL: https://www.lantmateriet.se/globalassets/kartor-och-geografisk-information/kartor/e_fastshmi.pdf.

[31] Swedish Land Survey, Laser Data Download, Forest, Technical Report, Swedish Land Survey, 2023, URL: https://www.lantmateriet.se/globalassets/geodata/geodataprodukter/hojddata/e_pb_laserdata_nedladdning_skog.pdf.

[32] G. Peronato, E. Rey, M. Andersen, 3D-modeling of vegetation from LiDAR point clouds and assessment of its impact on facade solar irradiation, Int. Arch. Photogramm. Remote. Sens. Spat. Inf. Sci. - ISPRS Arch. 42 (2W2) (2016) 67–70, http://dx.doi.org/10.5194/isprs-archives-XLII-2-W2-67-2016.

[33] D. Verma, O. Mumm, V.M. Carlow, Generating citywide street cross-sections using aerial LiDAR and detailed street plan, Sustain. Cities Soc. 96 (February) (2023) 104673, http://dx.doi.org/10.1016/j.scs.2023.104673.

[34] T.A.S. for Photogrammetry & Remote Sensing, LAS specification version 1.4 - R6, Am. Soc. Photogramm. Remote. Sens. (August) (2011) 1–18, URL: http://www.asprs.org/a/society/committees/lidar/LAS_1-4_R6.pdf.

[35] D. Lingfors, T. Johansson, J. Widén, T. Broström, Target-based visibility assessment on building envelopes: Applications to PV and cultural-heritage values, Energy Build. 204 (109483) (2019) 1–8, http://dx.doi.org/10.1016/j.enbuild.2019.109483, URL: https://www.sciencedirect.com/science/article/abs/

pii/S0378778819316433?via%3Dihub https://linkinghub.elsevier.com/retrieve/pii/S0378778819316433.

[36] D. Lingfors, J. Bright, N. Engerer, J. Ahlberg, S. Killinger, J. Widén, Comparing the capability of low- and high-resolution LiDAR data with application to solar resource assessment, roof type classification and shading analysis, Appl. Energy 205 (2017) 1216–1230, http://dx.doi.org/10.1016/j.apenergy.2017.08.045, URL: http://linkinghub.elsevier.com/retrieve/pii/S0306261917310619 https://linkinghub.elsevier.com/retrieve/pii/S0306261917310619.

[37] H. Huang, C. Brenner, M. Sester, A generative statistical approach to automatic 3D building roof reconstruction from laser scanning data, ISPRS J. Photogramm. Remote Sens. 79 (2013) 29–43, http://dx.doi.org/10.1016/j.isprsjprs.2013.02.004.

[38] L.-H. Björnsson, K. Morell, M.v. Noord, I. Pettersson, Solcellsparker i Sverige 2021 [PV Parks in Sweden 2021], Technical Report, RISE, 2022.

[39] R.E. Pawluk, Y. Chen, Y. She, Photovoltaic electricity generation loss due to snow – A literature review on influence factors, estimation, and mitigation, Renew. Sustain. Energy Rev. 107 (March) (2019) 171–182, http://dx.doi.org/10.1016/j.rser.2018.12.031.

[40] J.O. Street, R.J. Carroll, D. Ruppert, A note on computing robust regression estimates via iteratively reweighted least squares, Amer. Statist. 42 (2) (1988) 152–154, http://dx.doi.org/10.1080/00031305.1988.10475548.

[41] S. Jekal, J. Kim, D.H. Kim, J. Noh, M.J. Kim, H.Y. Kim, M.S. Kim, W.C. Oh, C.M. Yoon, Synthesis of LiDAR-detectable true black core/shell nanomaterial and its practical use in LiDAR applications, Nanomaterials 12 (20) (2022) http://dx.doi.org/10.3390/nano12203689.

[42] B. Espinar, L. Ramírez, A. Drews, H.G. Beyer, L.F. Zarzalejo, J. Polo, L. Martín, Analysis of different comparison parameters applied to solar radiation data from satellite and German radiometric stations, Sol. Energy 83 (1) (2009) 118–125, http://dx.doi.org/10.1016/j.solener.2008.07.009.

[43] J. Widén, M. Shepero, J. Munkhammar, On the properties of aggregate clear-sky index distributions and an improved model for spatially correlated instantaneous solar irradiance, Sol. Energy 157 (2017) 566–580, http://dx.doi.org/10.1016/j.solener.2017.08.033.

[44] T.H. Kolbe, G. Gröger, L. Plümer, CityGML: Interoperable access to 3D city models, in: P. van Oosterom, S. Zlatanova, E. Fendel (Eds.), Geo-Information for Disaster Management, Springer Berlin Heidelberg, Berlin, Heidelberg, 2005, pp. 883–899, http://dx.doi.org/10.1007/3-540-27468-5{_}63, URL: http://link.springer.com/10.1007/3-540-27468-5_63.

[45] T. Walla, J. Widén, J. Johansson, C. Bergerland, Determining and increasing the hosting capacity for photovoltaics in Swedish distribution grids, in: Proc. 27th European Photovoltaic Solar Energy Conference and Exhibition, 2012, pp. 4414–4420, http://dx.doi.org/10.4229/27thEUPVSEC2012-6DO.12.3.

[46] D. Lingfors, J. Marklund, J. Widén, Maximizing PV hosting capacity by smart allocation of PV: A case study on a Swedish distribution grid, in: Proceedings of 44th ASES Annual Conference, State College, PA, 2015.